An effective scheme of joint migration inversion in the pseudo-time domain

Qu, Shan; Verschuur, Dirk Jacob

DOI
10.1111/1365-2478.13296

Publication date
2022

Document Version
Final published version

Published in
Geophysical Prospecting

Received: 17 August 2021 | Accepted: 15 October 2022

DOI: 10.1111/1365-2478.13296

Geophysical Prospecting | EAGE EUROPEAN ASSOCIATION OF GEOSCIENTISTS & ENGINEERS

ORIGINAL ARTICLE

An effective scheme of joint migration inversion in the pseudo-time domain

Shan Qu | **Dirk Jacob Verschuur**

Laboratory of Acoustical Wavefield Imaging, Department of Applied Science, Delft University of Technology, Delft, The Netherlands

Correspondence
Shan Qu, Laboratory of Acoustical Wavefield Imaging, Department of Applied Science, Delft University of Technology, 2628 CJ Delft, The Netherlands.
Email: s.qu@tudelft.nl

Note that this paper is an extended version of work published in Qu et al. (2020) and Qu and Verschuur (2020). Moreover, parts of this work have been published in Qu (2020), in partial fulfillment of the requirements for the Ph.D. degree at Delft University of Technology.

Abstract

Traditional full-waveform inversion is a non-linear and ill-posed inversion problem. To reduce the non-linearity of it, joint migration inversion (joint migration inversion) was proposed as an alternative. Joint migration inversion tries to minimize the mismatch between measured and modelled reflection data. One key feature of joint migration inversion is its parameterization: two separate parameters, reflectivity (for the amplitudes of reflected events) and propagation velocity (for the phase effects). This separation helps to reduce the non-linearity of the inversion. During joint migration inversion, with the velocity being updated, the reflectors in the updated image are also shifting in depth accordingly, this phenomenon is called depth–velocity ambiguity. This interaction between the two parameters during inversion is desired to keep the image time consistent with the measured data but may lead to non-robustness of joint migration inversion due to the presence of local minima. Therefore, we propose a more robust joint migration inversion scheme, which parameterizes the models with vertical time, termed pseudo-time joint migration inversion. In pseudo-time, the updates of velocity will not result in the associated vertical location changes of reflectors in the estimated image. Instead, the reflectors are mainly getting more focused. One limitation is that the depth-pseudo-time conversion process assumes a simple linear relationship between depth and pseudo-time, which might cause some artefacts in the converted models when there exist strong lateral velocity variations. One subsequent round of depth joint migration inversion is recommended to resolve this issue. We demonstrate the effectiveness of our proposed method with a two-dimensional synthetic example in an extreme scenario, where the initial velocity model is homogeneous, a realistic offshore two-dimensional synthetic example, a two-dimensional field example from the Vøring basin in Norway and a simple three-dimensional synthetic example. In all examples, pseudo-time joint migration inversion manages to recover more reasonable updates in the inverted velocity and invert more focused reflectors in the inverted image, compared to depth joint migration inversion.

KEYWORDS
full waveform, imaging, inversion, Parameter estimation, seismics

INTRODUCTION

To recover more accurate subsurface images from the recorded seismic data in complex areas, a detailed velocity model is required. Therefore, a robust velocity inversion method that takes into account all the complex wave propagation and reflection phenomena in the seismic data is required.

Full waveform inversion (FWI) is a powerful inversion tool that provides a detailed velocity model by minimizing the misfit between recorded and predicted data in a least-squares sense (Tarantola, 1984). In FWI, the two-way wave equation can be solved via a finite-difference scheme with a parameterization of velocity. This non-linear two-way modelling makes FWI a non-linear and ill-posed inversion problem, and its non-convex objective function may suffer from local minima that are not informative about the true parameters (Symes, 2008; Virieux & Operto, 2009). Internal multiples and transmission effects are in principle properly considered. However, density variations are usually not considered in FWI, thus compensated by velocity variations. To partly avoid these issues, FWI is usually only applied to diving waves or the low-frequency part of the data and starts from a sufficiently good input velocity model (Operto et al., 2004; Plessix et al., 2010). To mitigate these issues, Xu et al. (2012) propose reflection FWI to invert long-wavelength components of the velocity by using the modelled reflected wavefields generated from images. However, it has the problem of using one inversion parameter to explain both the reflection and propagation effects in the data, making the inversion even more non-linear (Berkhout, 2014c; Qu, 2020; Verschuur et al., 2016). Moreover, the computational effort of (reflection) FWI grows exponentially with increasing frequency, which makes it difficult to handle high frequencies.

Joint migration inversion (JMI) was proposed as an alternative velocity inversion method to overcome the aforementioned limitations in FWI (Berkhout, 2014b; Qu, 2020; Qu & Verschuur, 2020; Staal, 2015; Verschuur et al., 2016). JMI automatically inverts both reflectivity and propagation velocity model in a least-squares sense. The forward modelling of JMI – full wavefield modelling – simulates the data in a way that amplitudes are defined by the estimated reflectivities, whereas travel times are separately controlled by the velocity model (Berkhout, 2014a). Thus, JMI takes into account transmission effects and surface/internal multiples (Berkhout, 2014b). It is also cost-effective because its modelling is not based on the finite-difference algorithm. Due to its scale separation of parameters, JMI is more linear than FWI (Verschuur et al., 2016). However, JMI fails to image steep dips without modifications (Davydenko et al., 2014). Note that both JMI and FWI have their advantages and shortcomings and combining FWI and JMI seems to give improved results (Davydenko & Verschuur, 2017a; Eisenberg et al., 2019; Sun et al., 2018a, 2018b).

Currently in JMI, the reflectivity and velocity updates are employed in an alternating manner. The reflectivity updates in JMI are always located at certain depth levels to maximize the overlap between measured and modelled data. Therefore, changes in the velocity model also result in location changes of reflectors, termed depth–velocity ambiguity. For example, in the case of a lower velocity model (lower than the true values), the reflectors are estimated at shallower depth levels, and vice versa, a higher velocity model will estimate too large reflector depths. During inversion, with the velocity model being updated, the reflectors in the calculated reflectivity model are also shifting accordingly. This kind of interaction between image and velocity models during inversion is needed to keep the image time consistent with the measured data, however, may also lead to non-robustness of JMI due to the presence of local minima. Therefore, a more robust JMI scheme, in which the reflector locations in the calculated image are less dependent on the velocity updates, is desired.

To reduce the computational overhead due to the spatial over-sampling of deep layers in depth migration, Ma and Alkhalifah (2012, 2013) propose to implement reverse-time migration in the pseudo-time domain, which means the estimated image is parameterized with vertical time. The vertical time of the pseudo-time domain is equal to the integral over depth of the vertical slowness. Therefore, the wavelength remains constant in spite of the vertical velocity variation. To tackle the depth–velocity ambiguity in FWI, Plessix et al. (2012) and Plessix (2013) propose to apply FWI in the pseudo-time domain, in which a more robust velocity update can be obtained because the vertical locations of large velocity discontinuities are less dependent on velocity in vertical time than in depth. In the context of JMI, the locations of reflectors in the estimated reflectivity model will also be less dependent on the velocity updates during inversion in pseudo-time.

Therefore, in this work, we propose a more robust JMI scheme, which parameterizes the reflectivity and velocity models with vertical time, termed pseudo-time JMI. In this way, the updates in the velocity model during inversion will not result in large location changes of reflectors in the estimated image. Instead, the reflectors are getting more focused gradually at the same vertical time levels.

This paper is organized as follows: we first recap some theoretical details of depth JMI, then describe it in the pseudo-time domain. In the end, we demonstrate the effectiveness of our proposed method using a two-dimensional (2D) synthetic example in an extreme scenario, where the initial velocity model has a constant value, a realistic 2D synthetic example, a 2D field data example from the Vøring basin in Norway, and a simple three-dimensional synthetic example. Note that this paper is an extended version of work published in Qu et al. (2020) and Qu and Verschuur (2021).

THEORY OF DEPTH JOINT MIGRATION INVERSION

Full wavefield modelling

The flow diagram of the joint migration inversion (JMI) process is shown in Figure 1. The core of JMI is its forward modelling process named full wavefield modelling (FWMod). FWMod is based on a parameterization of reflectivity and propagation velocity (Berkhout, 2014a). Both multiples and transmission effects are considered in FWMod. In the depth domain, the model space (x, y, z) is divided into a fine set of depth levels $z_m, m = 0, \ldots, N_z - 1$ with Δz spacing. N_x and N_y represent the number of cells in the x- and y-directions, respectively. For each layer, reflectivity and propagation velocity are defined and four wavefields are calculated – the down-going and up-going incoming wavefield $\mathbf{p}^+$ and $\mathbf{p}^-$ and the down-going and up-going outgoing wavefield $\mathbf{q}^+$ and $\mathbf{q}^-$. Note that for our mathematical description we consider one frequency slice and one shot, which are independent of each other. Therefore, it is easy to extend this theory to the full frequency and full shots case. The dimension of the monochromatic wavefields $\mathbf{p}^\pm$ and $\mathbf{q}^\pm$ is $(N_x \times N_y \times N_z)$. The building blocks of FWMod, illustrated in Figure 2, consist of two parts: reflection and transmission at each level and propagation in-between two conjunctive levels, controlled by propagation velocity.

(1) Reflection and transmission at each level. At z_m, reflected wavefields are described via downwards/upwards reflectivity operators $\mathbf{R}^{\cup/\cap}(z_m)$ and transmissions are described via down-/up-going transmission operators $\mathbf{T}^{+/-}(z_m)$. The dimension of $\mathbf{R}^{\cup/\cap}(z_m)$ and $\mathbf{T}^{\pm}(z_m)$ is $(N_x \times N_y) \times (N_x \times N_y)$. The wavefields at z_m are connected by these reflectivity and transmission operators (Berkhout, 2014a; Davydenko & Verschuur, 2017b):

$$\begin{aligned}\mathbf{q}^+(z_m) &= \mathbf{T}^+(z_m)\mathbf{p}^+(z_m) + \mathbf{R}^\cap(z_m)\mathbf{p}^-(z_m),\\ \mathbf{q}^-(z_m) &= \mathbf{T}^-(z_m)\mathbf{p}^-(z_m) + \mathbf{R}^\cup(z_m)\mathbf{p}^+(z_m).\end{aligned} \tag{1}$$

Note that the complete version of $\mathbf{R}(z_m)$ represents spatial convolution operators that can implicitly apply a reflection coefficient dependent on the incident angle of the waves (Berkhout, 2014c; Davydenko & Verschuur, 2017b). Therefore, it can handle angle-dependent reflection. However, this complete version of reflection operators leads to a large solution space and would put the inversion in danger of overparameterization, if propagation velocities are also updated. Thus, in this work, we make an assumption of scalar reflectivity operators by ignoring the influences of incident angles and using only the diagonal values. As a result, this version of JMI cannot easily handle large-offset data due to the angle-versus-offset (AVO) effects (Sun et al., 2019). The strategy we use to handle this AVO issue in JMI will be discussed later.

(2) Propagation in-between two conjunctive levels In-between z_m and z_{m+1}, the propagation of wavefields is described via down- and up-going propagation operators $\mathbf{W}(z_{m+1}, z_m)$ and $\mathbf{W}(z_m, z_{m+1})$. The four wavefields at z_m and z_{m+1} are connected by these propagation operators (Berkhout, 2014a; Qu, 2020):

$$\begin{aligned}\mathbf{p}^+(z_{m+1}) &= \mathbf{W}(z_{m+1}, z_m)\mathbf{q}^+(z_m),\\ \mathbf{p}^-(z_m) &= \mathbf{W}(z_m, z_{m+1})\mathbf{q}^-(z_{m+1}).\end{aligned} \tag{2}$$

By assuming the medium in between each two consecutive levels being locally homogeneous, we can relate one row of the propagation operator $\mathbf{W}(z_{m+1}, z_m)$ to a phase-shift operator that propagates the wavefields from one depth level (z_m) to one point at the next depth level (x_l, y_n, z_{m+1}) (Gazdag, 1978):

$$\begin{aligned}\mathbf{w}^\dagger_{l,n}(z_{m+1}, z_m) &= \mathcal{F}^{-1}_{x,y}\left[e^{-jk_z\Delta z}e^{jk_x x_l}e^{jk_y y_n}\right],\\ k_z &= \begin{cases}\sqrt{k^2 - k_x^2 - k_y^2} & \sqrt{k_x^2 + k_y^2} \le |k|\\ -j\sqrt{k_x^2 + k_y^2 - k^2} & \sqrt{k_x^2 + k_y^2} > |k|,\end{cases}\\ &\text{with } k = \frac{\omega}{v_{l,n}(z_m)},\end{aligned} \tag{3}$$

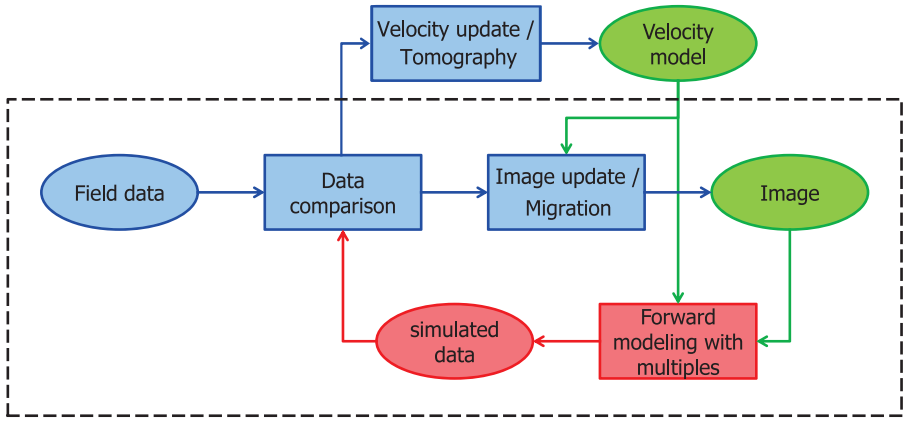

FIGURE 1 JMI flow chart, where both velocities and reflectivities (i.e., the image) are updated (Verschuur & Staal, 2014)

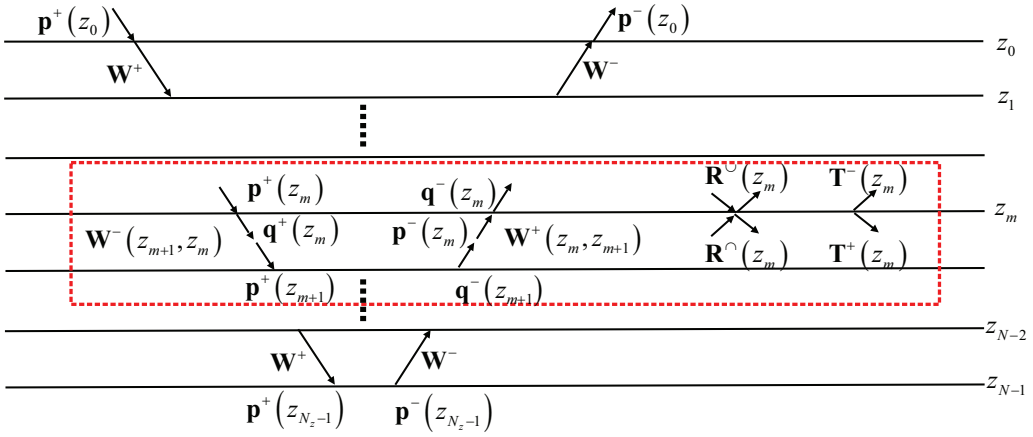

FIGURE 2 A schematic illustration of FWMod in depth. For the mth building block highlighted with a red square, $\mathbf{p}^{\pm}$ are the incoming down-/up-going wavefields and $\mathbf{q}^{\pm}$ are the outgoing down-/up-going wavefields; $\mathbf{R}^{\cap/\cup}$ and $\mathbf{T}^{\pm}$ denote downwards/upwards reflectivity and down-/up-going transmission operators, respectively; $\mathbf{W}(z_{m+1}, z_m)$ and $\mathbf{W}(z_m, z_{m+1})$ represent the down-/up-going propagation operators.

where $\mathcal{F}_{x,y}^{-1}$ is the inverse spatial Fourier transform from (k_x, k_y) to the (x, y). j denotes the imaginary unit. $v_{l,n}(z_m)$ is a scalar, representing the propagation velocity at the location (x_l, y_n, z_m).

Based on the current reflectivity and propagation velocity model, by extrapolating the wavefields downwards from z_0 to z_{N_z-1} and then upwards from z_{N_z-1} to z_0 with the aforementioned building blocks shown in Figure 2, one round-trip of modelling is constructed, yielding only primaries. Subsequently, based on the updated wavefields, the next round-trip of modelling is constructed, after which the first order of internal multiples is included, etc. Note that FWMod based on these building blocks is flexible and can be easily extended to include more physics by upgrading the building block (Alshuhail & Verschuur, 2019; Alasmri & Verschuur, 2019).

Inversion

During inversion, the subsurface parameters are updated iteratively by fitting the modelled wavefield to the measured wavefield in a least-square sense. The following objective function is defined at the surface:

$$J = \frac{1}{2} \sum_{\omega} \sum_{\text{shots}} ||\mathbf{d}_0^- - \mathbf{p}^-(z_0)||_2^2, \tag{4}$$

where $||.||_2^2$ describes the sum of the squares of the values. $\mathbf{d}_0^-$ is the measured wavefields at the surface (the up-going component, after receiver deghosting for marine data). The gradient calculation of the reflectivity and velocity based on objective function (4) involves a reverse extrapolation of the wavefield residual and several cross-correlation operations (Qu, 2020; Qu & Verschuur, 2020; Staal & Verschuur, 2013; Sun et al., 2019; Verschuur et al., 2016). After the gradients are calculated, the parameters are updated and the residual wavefields are slowly driven to a minimum level (Staal & Verschuur, 2013). The flow diagram of the inversion process is shown in Figure 1.

One key feature of JMI is its parameterization: two separate parameters – **r** and **v** – have different effects on the modelled data; the reflectivities are responsible for the amplitudes of the reflected events, and the propagation velocity is responsible for the phase effects of them (i.e., the arrival time). Currently, the reflectivity and velocity models are updated alternately. The reflectivity updates in JMI are always located at certain depth levels to maximize the overlap between the measured and modelled data. Therefore, changes in the velocity model result in the associated changes in the reflector locations. One small-scale test regarding this interaction is shown in Figures 3a–d. By comparing Figure 3b,d with Figure 3a,c, it can be observed that in the case where the velocities are much lower than the true velocities, reflectors are estimated at shallower depth levels. This kind of interaction is also called depth–velocity ambiguity. It may lead to the non-robustness of JMI during inversion. Therefore, a more robust JMI scheme, in which the reflector locations in the inverted image are less dependent on the velocity updates, is desired.

THEORY OF PSEUDO-TIME JOINT MIGRATION INVERSION

To avoid the non-robustness in joint migration inversion (JMI) due to the depth–velocity ambiguity, we propose a more robust JMI scheme, which parameterizes the models with vertical time, termed pseudo-time JMI. Given the current

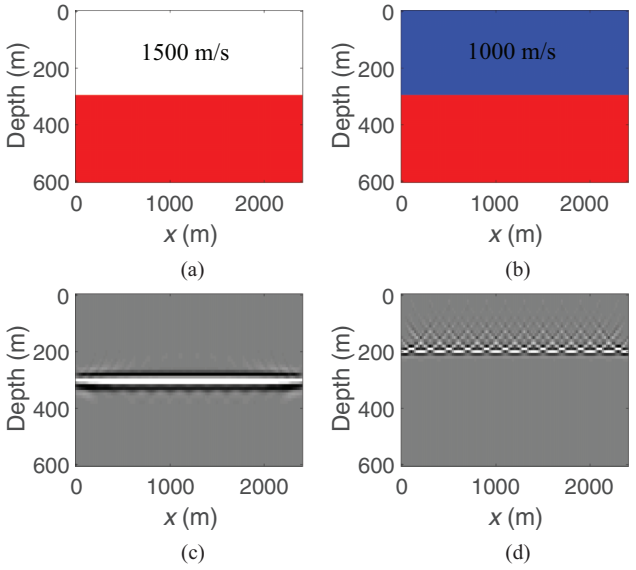

FIGURE 3 A small-scale test to show the benefit of inversion in the pseudo-time domain. In depth: (a) and (b) the true velocity model and a wrong velocity model with lower value, (c) and (d) the associated images.

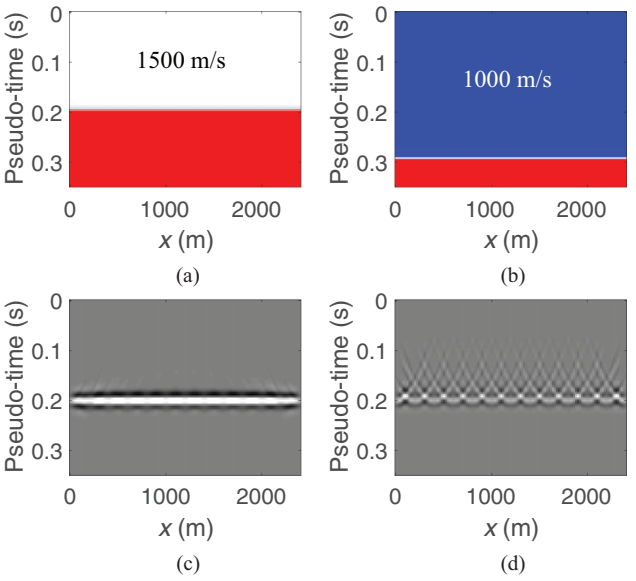

FIGURE 4 A small-scale test to show the benefit of doing inversion in the pseudo-time domain. In pseudo-time: (a) and (b) the models converted from Figure 4a,b and (c) and (d) the associated image models.

velocity model in depth $\mathbf{v}(z)$, the vertical time is defined by

$$\tau = \int_0^z \frac{\mathrm{d}z'}{\mathbf{v}(z')}, \tag{5}$$

and the inverse relation is

$$z = \int_0^\tau \mathbf{v}(\tau')\mathrm{d}\tau' \tag{6}$$

(Ma & Alkhalifah, 2012, 2013). The vertical locations of reflectors are supposed to be less dependent on the velocity in the pseudo-time domain than in the depth domain. To demonstrate this, a same small-scale test is carried out in the pseudo-time domain and shown in Figure 4a–d. We notice that the error in the velocity model does not result in location changes of reflectors in the associated image in the pseudo-time domain. Instead, the reflectors are just less focused in the presence of velocity errors. In addition, the wavelength in the pseudo-time domain remains constant despite the vertical velocity variations; therefore, pseudo-time inversion also helps to reduce the computational overhead due to the spatial over-sampling of deep layers (Ma & Alkhalifah, 2012, 2013).

The theory of pseudo-time full-wavefield modelling (FWMod) and JMI is quite straightforward and can be realized easily with very few changes to the existing depth domain code. Instead of defining models and wavefields in space (x, z), they are defined in the space (x, τ). The model space is divided into a fine set of pseudo-time levels $\tau_m, m = 0, \ldots, N_\tau - 1$ separated by a small distance $\Delta\tau$ along a certain spatial direction $\tau-$axis. The schematic illustration of pseudo-time FWMod is shown in Figure 5. The building blocks in the pseudo-time domain – reflection and transmission at each level and propagation in-between two conjunctive levels – can be expressed as

$$\begin{aligned}\mathbf{q}^+(\tau_m) &= \mathbf{T}^+(\tau_m)\mathbf{p}^+(\tau_m) + \mathbf{R}^\cap(\tau_m)\mathbf{p}^-(\tau_m),\\ \mathbf{q}^-(\tau_m) &= \mathbf{T}^-(\tau_m)\mathbf{p}^-(\tau_m) + \mathbf{R}^\cup(\tau_m)\mathbf{p}^+(\tau_m).\end{aligned} \tag{7}$$

$$\begin{aligned}\mathbf{p}^+(\tau_{m+1}) &= \mathbf{W}(\tau_{m+1}, \tau_m)\mathbf{q}^+(\tau_m),\\ \mathbf{p}^-(\tau_m) &= \mathbf{W}(\tau_m, \tau_{m+1})\mathbf{q}^-(\tau_{m+1}).\end{aligned} \tag{8}$$

Here, the propagation operator in pseudo-time, adapted from Equation (3), can be written as

$$\begin{aligned}\mathbf{w}^\dagger_{l,n}(\tau_{m+1}, \tau_m) &= \mathcal{F}^{-1}_{x,y}\left[\mathrm{e}^{-jk_z\Delta\tau v_{l,n}(\tau_m)}\mathrm{e}^{jk_x x_l}\mathrm{e}^{jk_y y_n}\right],\\ k_z &= \begin{cases}\sqrt{k^2 - k_x^2 - k_y^2} & \sqrt{k_x^2 + k_y^2} \le |k|\\ -j\sqrt{k_x^2 + k_y^2 - k^2} & \sqrt{k_x^2 + k_y^2} > |k|,\end{cases}\\ &\text{with } k = \frac{\omega}{v_{l,n}(\tau_m)}.\end{aligned} \tag{9}$$

During inversion, the subsurface models in pseudo-time are optimized by fitting the measured wavefield with the modelled wavefield, which is also generated recursively in the pseudo-time domain. Note that, similar to depth JMI, fine details are not expected in the inverted velocity using pseudo-time JMI, as it only explains the propagation effects in the data. After the process of pseudo-time JMI, the inverted

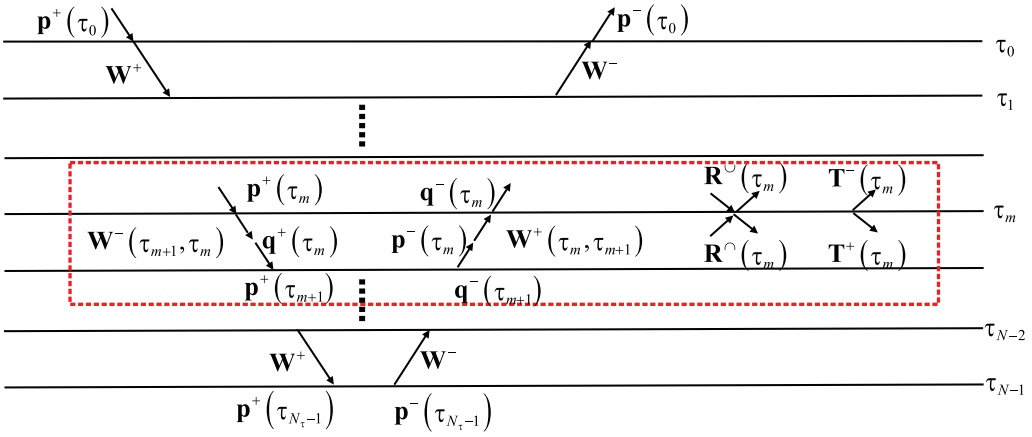

FIGURE 5 A schematic illustration of FWMod in pseudo-time. For the *m*th building block highlighted with a red square, $\mathbf{p}^{\pm}$ are the incoming down-/up-going wavefields and $\mathbf{q}^{\pm}$ are the outgoing down-/up-going wavefields; $\mathbf{R}^{\cap/\cup}$ and $\mathbf{T}^{\pm}$ denote downwards/upwards reflectivity and down-/up-going transmission operators, respectively; $\mathbf{W}(\tau_{m+1},\tau_m)$ and $\mathbf{W}(\tau_m,\tau_{m+1})$ represent the down-/up-going propagation operators.

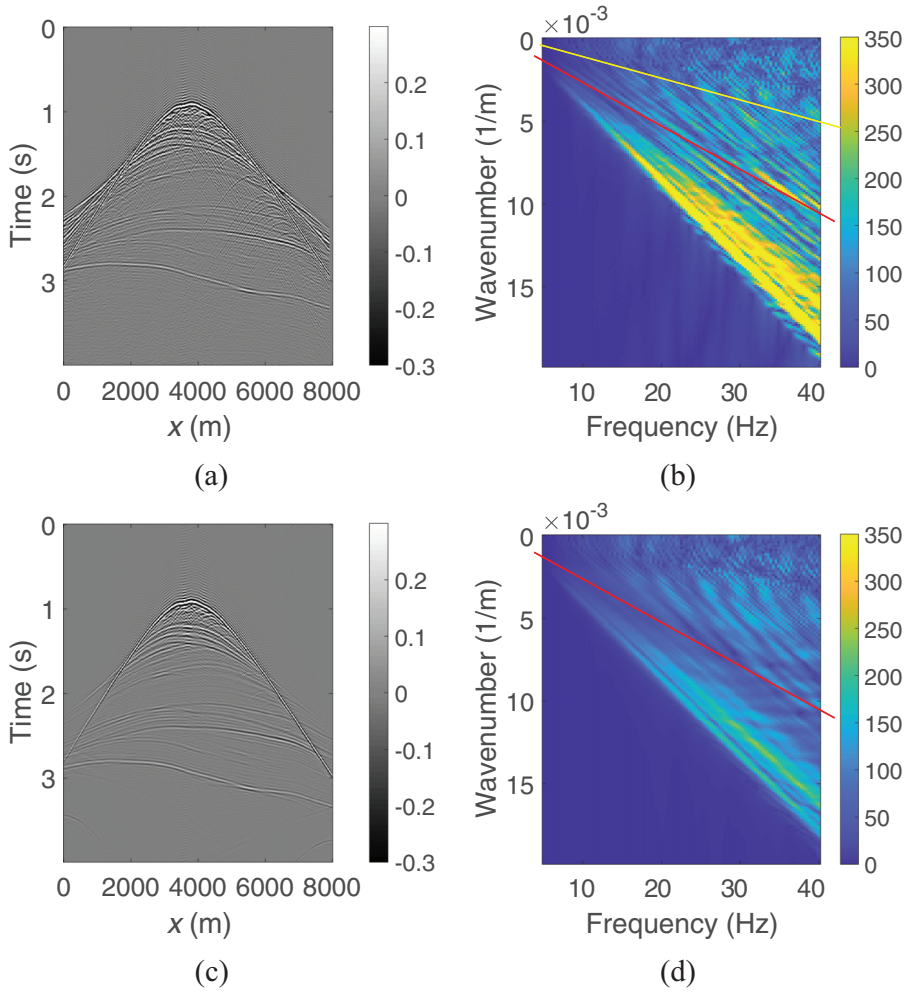

FIGURE 6 Middle shot profile comparison in the T–X domain and F–K domain before AVO mitigation based on the subsurface model in Figure 10a. (a) and (b) generated via FD modelling; (c) and (d) generated via angle-independent FWMod.

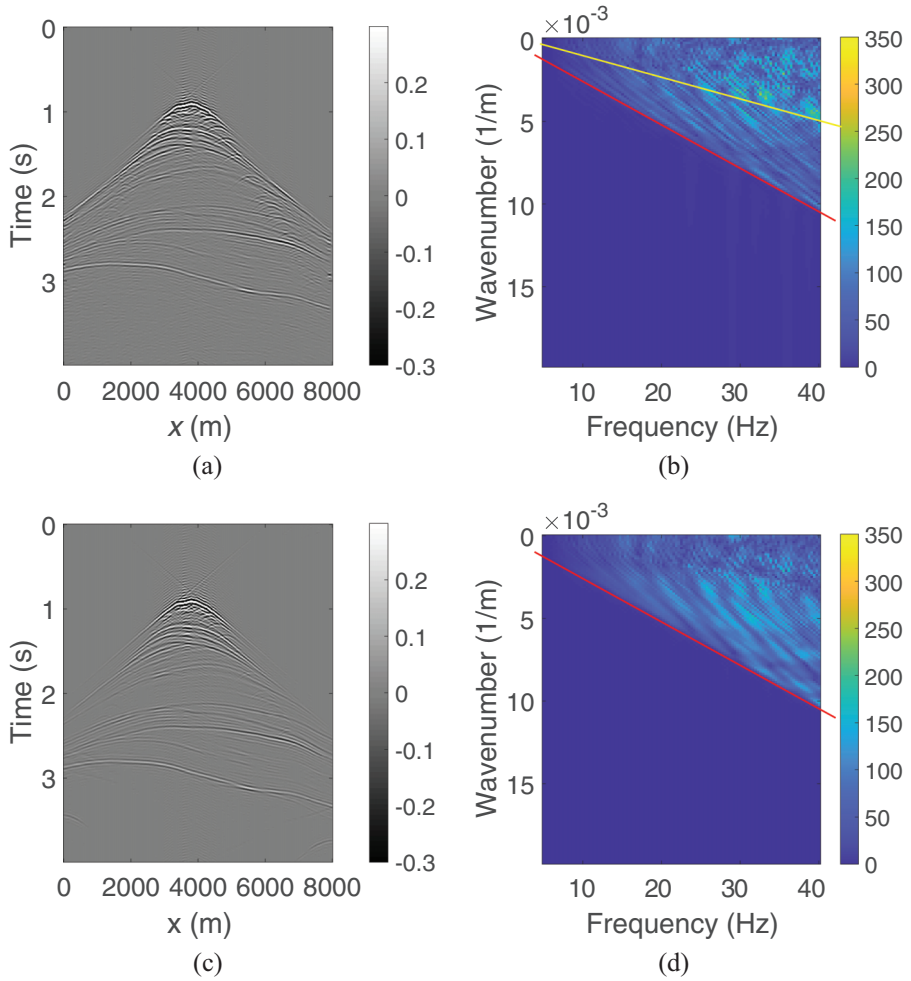

FIGURE 7 Middle shot profile comparison in the T–X domain and F–K domain after AVO mitigation based on the subsurface model in Figure 10a. (a) and (b) the filtered and scaled version of Figure 6a,b; (c) and (d) the filtered version of Figure 6c,d.

models are converted back to the depth domain. Due to the imperfect inverted velocity via pseudo-time JMI and the simple linear relationship between depth and pseudo-time, there might be some artefacts in the converted models, especially in the presence of strong lateral velocity variations in the subsurface. To resolve this issue, an additional step of depth JMI is required with a smoothed version of the inverted velocity via pseudo-time JMI as the starting model.

One additional concern in the current JMI implementation (for both depth and pseudo-time JMI) is that, due to the scalar reflectivity assumption, the current JMI cannot correctly match the part of the measured data at large offsets due to strong angle-versus-offset (AVO) effects (Sun et al., 2019). To illustrate this, a comparison of shot profiles is shown in Figure 6a,c, which are generated using finite-difference (FD) modelling and angle-independent FWMod based on the subsurface model in Figure 10, respectively. We can see the high amplitudes at larger offsets in the FD-modelled data, whereas, angle-independent FWMod is not able to generate these AVO effects. The same effect can be observed in the F–K (frequency–wavenumber) domain in Figure 6b,d. It can be seen that the part of signals below the red line in Figure 6b contains strong AVO effects. The part between the red and yellow lines also has AVO effects, although not as strong. Based on the above observations, we choose to use a robust AVO mitigating workflow, which consists of two additional processing steps in the data comparison during inversion and an F–K filtering process to cut off the strong AVO effects (signals below the red line) in the measured and modelled data; an F–K scaling to further scale down the remaining AVO effects in the measured data (signals between the red and yellow lines). By comparing Figure 6b and 6d, it can be seen that the F–K scaling is expected to decay the amplitude of the FD data exponentially along the wavenumber and frequency axes in the area between the red and yellow lines. Therefore, inspired by how evanescent waves decay in the F–K domain, we pragmatically design the F–K scaling as $e^{-\sqrt{\mathbf{k_x}^2+\mathbf{k_y}^2-w^2/v^2}\Delta z}$. The demonstration of this processing step on the seismic data is shown in Figure 7a–d, in which we chose the initial velocity

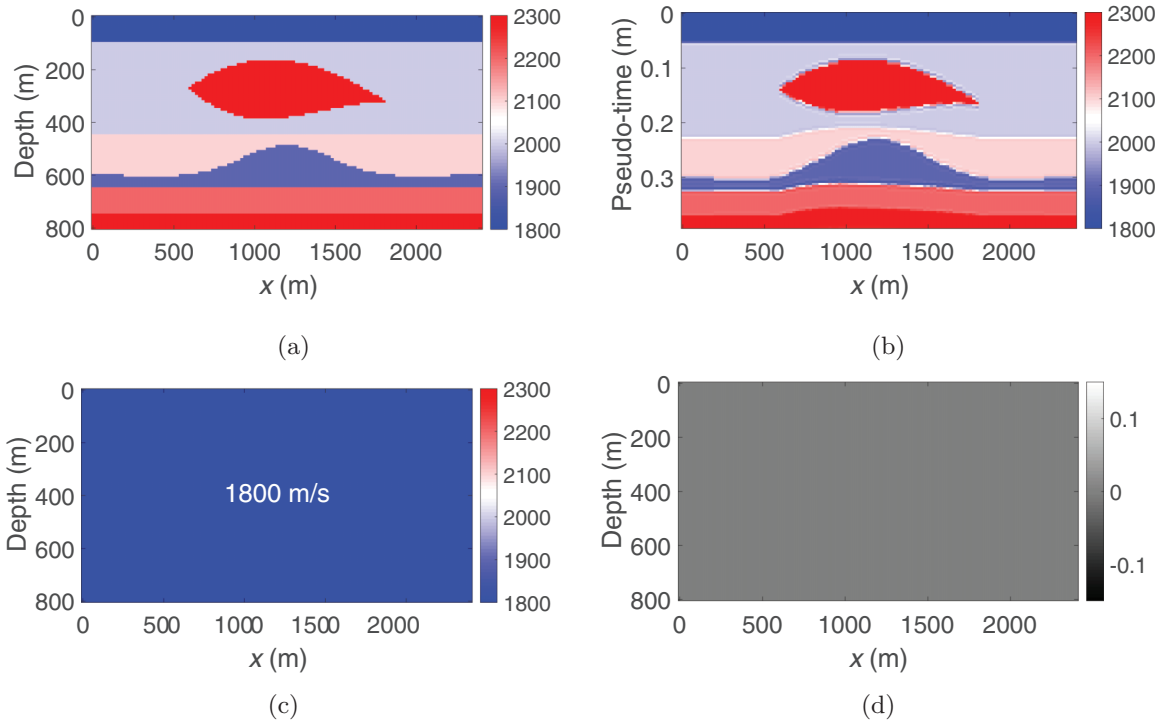

FIGURE 8 A synthetic example with a large velocity error: (a) and (b) true velocity model in depth and pseudo-time; (c) and (d) initial velocity and reflectivities

value at 1100 m depth level (2915 m/s) for the F–K filtering and the maximal initial velocity value (6582 m/s) for the F–K scaling. During JMI, we use the residual between the processed measured and modelled data to calculate the model gradients at each iteration.

EXAMPLES

A synthetic data example in an extreme scenario

To demonstrate the effectiveness of our proposed method, we first present a synthetic example in an extreme scenario to show the advantages and disadvantages of the proposed pseudo-time joint migration inversion (JMI). The dataset is generated via full wavefield modelling (FWMod) based on the true velocity model in Figure 8a. Figure 8b shows the true velocity model in the pseudo-time domain, which is converted from Figure 8a using Equation (5). Note that this true velocity model in pseudo-time is just for demonstrating purpose and not used in the generation of data. The source and receiver spacings are 200 and 20 m, respectively. We use a Ricker wavelet with a 20-Hz peak frequency, and the frequency bandwidth during JMI is 5-40 Hz. Forty iterations in a gradient descent scheme are applied in a multi-scale way for both depth and pseudo-time JMI. The initial models are shown in Figure 8c,d, the initial reflectivities are zero and the initial velocity model is set to a constant value of 1800 m/s. Note that, for comparison, the implementations of depth JMI and pseudo-time JMI share the same other settings, for example, $N_z = N_\tau$, and this is the case for all the other examples in this section.

By starting from an extremely erroneous initial velocity model, the traditional depth JMI fails to give reasonable results, which are shown in Figure 9a,b. Thanks to the improved robustness, JMI in the pseudo-time domain manages to recover a high-quality image (Figure 9d), when compared to the true velocity model in pseudo-time shown in Figure 8b. It means that the estimated velocity in Figure 9c is good enough to explain the propagation effects in the data. However, it does not show details because it can only explain the propagation effects in the data. After the process of pseudo-time JMI, the inverted models are converted back to the depth domain (Figure 9e,f). We notice the undulations of the deeper reflectors because the conversion from pseudo-time into depth is not perfect due to the imperfect estimated velocity. To resolve this issue, one extra round of depth JMI is applied with the inverted velocity model in Figure 9e (achieved by pseudo-time JMI) as the starting model. The final results are shown in Figure 9g,h, in which the reflectors are not wiggled any more.

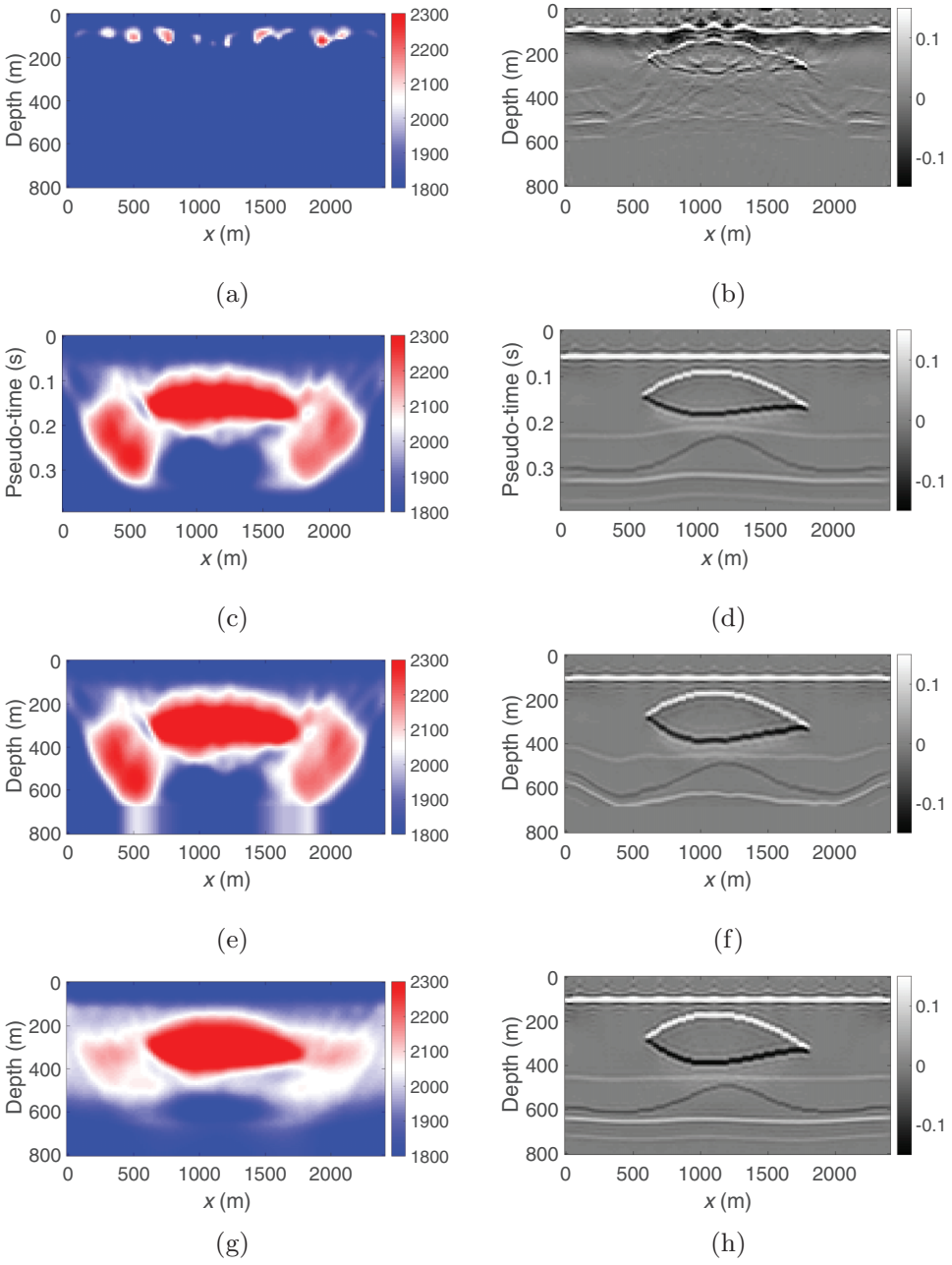

FIGURE 9 A synthetic example with a large velocity error: (a) and (b) The inverted velocity and reflectivities using depth JMI; (c) and (d) the inverted velocity and reflectivities using pseudo-time JMI; (e) and (f) the corresponding models in depth, which are converted from (c) and (d); (g) and (h) the inverted velocity and reflectivities using depth JMI starting with the velocity model (c).

A realistic two-dimensional offshore synthetic data example

To further demonstrate the effectiveness of the proposed JMI scheme, we revisit a realistic two-dimensional (2D) deep water synthetic dataset used in Sun et al. (2019), in which the original JMI implementation failed to give reasonable velocity updates when starting from a poor initial velocity. This synthetic subsurface model was built via known geological information. The true velocity model is shown in Figure 10a, and the corresponding density model is generated via Gardner's equation except for the water layer. The measured data shown in Figure 6a are generated using acoustic finite-difference (FD) modelling based on both density and velocity models with a 15-Hz Ricker wavelet, and the reliable frequency spectrum is 5–40 Hz. The receivers with 25 m spacing and the sources with 100 m spacing are located along the entire surface. A gradient descent scheme

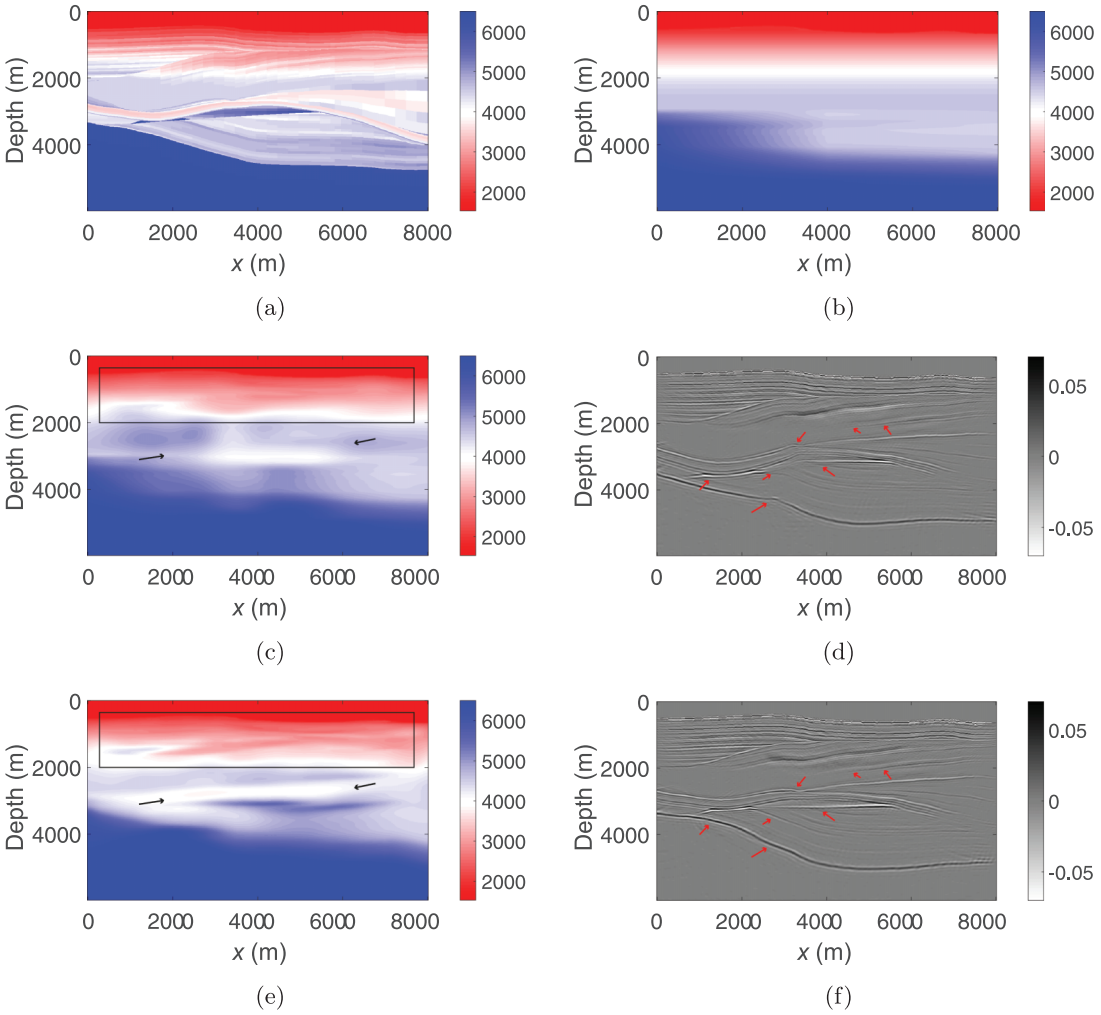

FIGURE 10 A realistic synthetic example: (a) and (b) true and initial velocity model; (c) and (d) the inverted velocity and image using depth JMI; (e) and (f) the inverted velocity and image using pseudo-time JMI. Note that one extra round of depth JMI is applied after pseudo-time JMI.

with 240 iterations is applied in a multi-scale manner for both depth and pseudo-time JMI.

The initial reflectivities are zero, and the initial velocity is a smooth starting model, as shown in Figure 10b. The inverted models using depth JMI are shown in Figure 10c,d. It can be seen that the update is not very effective, especially in the deeper part. The inverted results using the proposed pseudo-time JMI are shown in Figure 10e,f. We can observe that this proposed JMI scheme achieves much better results regarding both velocity and image. Figure 10e exhibits much more details in the shallow area and manages to recover the velocity inversion at a depth of approximately 3000 m (the above-mentioned improvements are pointed out by black arrows and square in Figure 10c,e. Moreover, the reflectors in the corresponding image (Figure 10f) are better focused compared to the ones using depth JMI in Figure 10d (some improvements are highlighted with red arrows). Note that one extra round of depth JMI is applied in the final step of processing. In the end, we show in Figure 11a,b the data differences between the filtered and scaled measured data (shown in Figure 7a) and the modelled data based on the inverted models, where some improvements are highlighted with a red square. It can be clearly observed that pseudo-time JMI can predict the data much better than depth JMI.

Field data example based on a deepwater marine dataset from the Vøring basin in Norway

In this subsection, we demonstrate the proposed method on a 2D field dataset from the Vøring basin. The data were acquired by a streamer survey in the North Sea, in the Vøring area, offshore Norway. The source and receiver spacings used in our example are 50 and 25 m, respectively. Several preprocessing steps have been applied to the data, including the direct wave and surface-related multiple removals, deghosting, near-offset interpolation and using reciprocity to

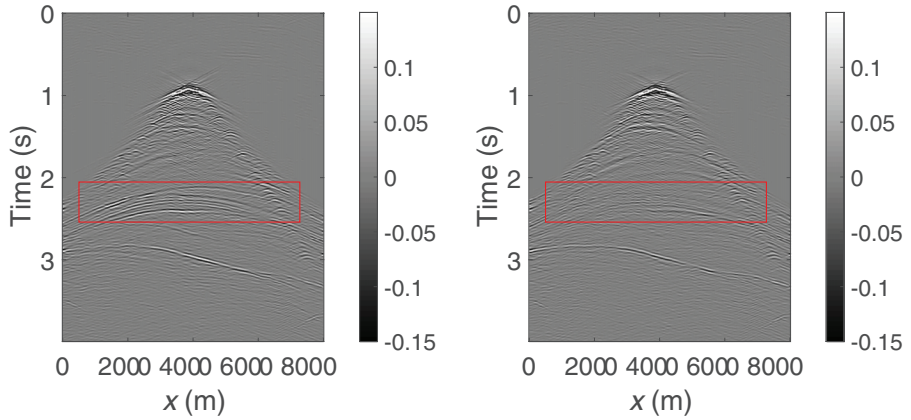

FIGURE 11 A realistic synthetic example: difference for one shot record between the measured data (Figure 7a) and modelled data based on the inverted models using depth JMI (a) and pseudo-time JMI (b). Note the different amplitude scales in (a) and (b) compared to Figure 7a.

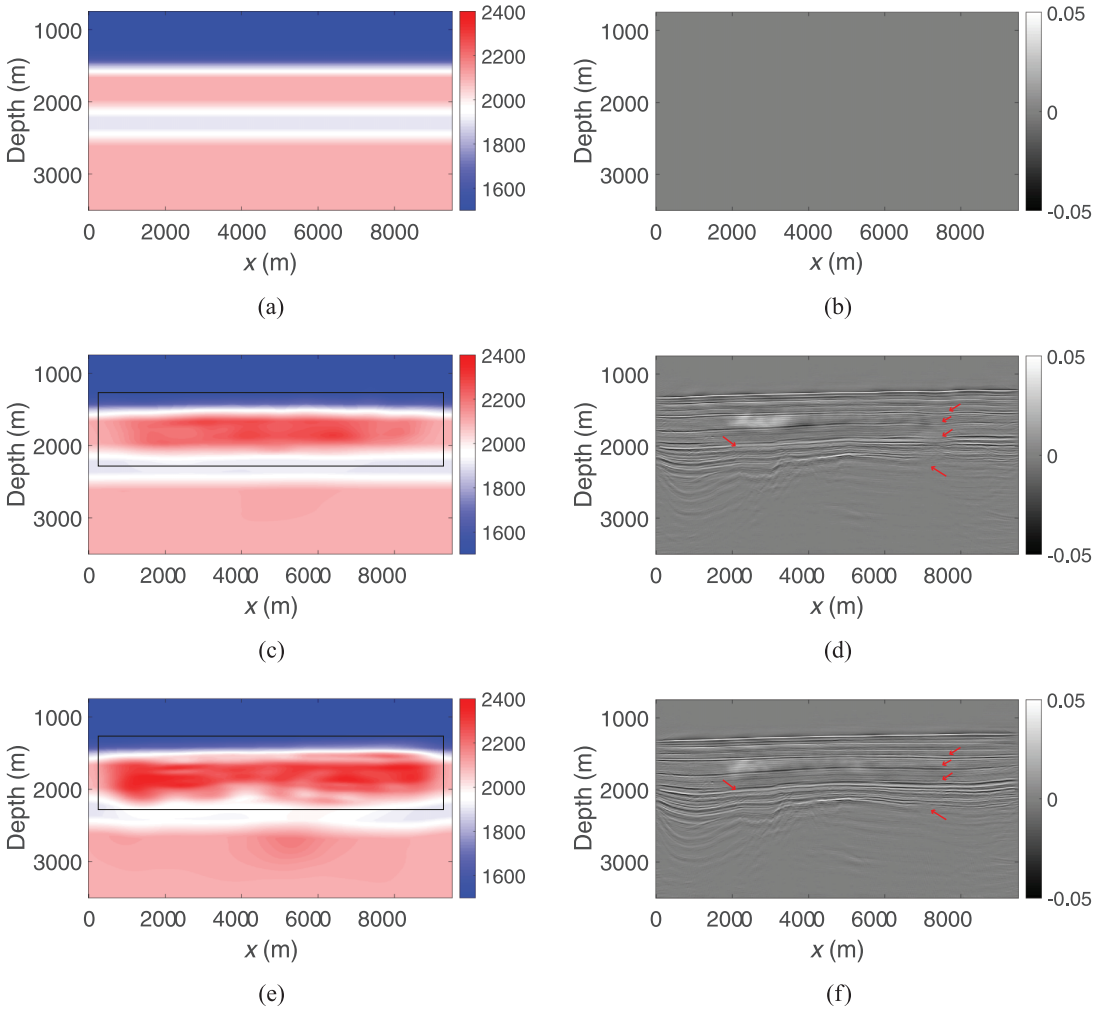

FIGURE 12 Field example: (a) and (b) initial velocity and reflectivities; (c) and (d) the inverted velocity and reflectivities using depth JMI; (e) and (f) the inverted velocity and reflectivities using pseudo-time JMI

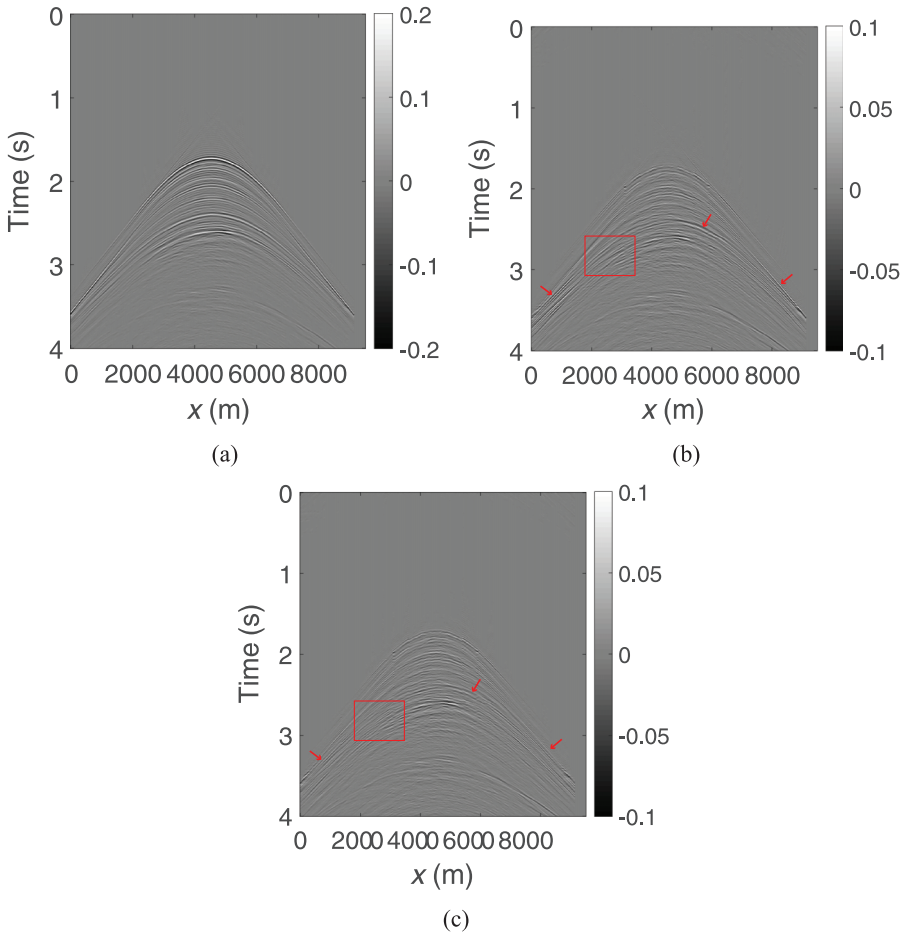

FIGURE 13 Field example for one shot record: the measured data (a) and the corresponding data difference with the modelled data based on the inverted models using depth JMI (b) and pseudo-time JMI (c). Note the different amplitude scale in (b) and (c) compared to (a).

make the shot records split spread. The source wavelet was estimated from the surface-related multiples by using a so-called estimation of primaries by sparse inversion process (van Groenestijn & Verschuur, 2009). The frequency bandwidth during JMI is 5–40 Hz. Figure 12a shows the initial velocity model obtained by normal moveout analysis, and the initial reflectivity model is zero (Figure 12b). The input initial velocity for pseudo-time JMI is the model converted from Figure 12a into the pseudo-time domain, and the initial reflectivities are also zero. A gradient descent scheme with 80 iterations is applied in a multi-scale way for both depth and pseudo-time JMI.

The inverted results using depth JMI are shown in Figure 12c,d, and the results using pseudo-time JMI are displayed in Figure 12e,f. From these figures, the same observation can be drawn as for the previous synthetic example: The updates via depth JMI alone is not effective (Figure 12c); in comparison, the inverted velocity using the proposed pseudo-time JMI shows more reasonable updates (Figure 12e). The improvement can be observed clearly at depth 1500–2200m, which is highlighted via a black square. Moreover, the reflectors inverted using pseudo-time JMI in Figure 12f are better focused compared to the inverted ones using depth JMI in Figure 12d. Some improvements are highlighted with red arrows in the inverted images. In the end, a measured shot profile is shown in Figure 13a, and the corresponding data difference between the measured data and modelled data based on depth and pseudo-time JMI is shown in Figure 13b,c. It can be observed that pseudo-time JMI can reconstruct the data much better than depth JMI (highlighted with red square and arrows).

DISCUSSION

The full wavefield modelling (FWMod) and joint migration inversion (JMI) process in the depth domain and pseudo-time domain can be straightforwardly extended to a full three-dimensional (3D) situation. In this discussion, we show the potential effectiveness of the proposed method for a 3D case based on a simple synthetic model (Figure 14a). This 3D synthetic model is an extended version of the two-dimensional model shown in Figure 8a. The dataset is generated via 3D FWMod. The inline source and receiver spacings are

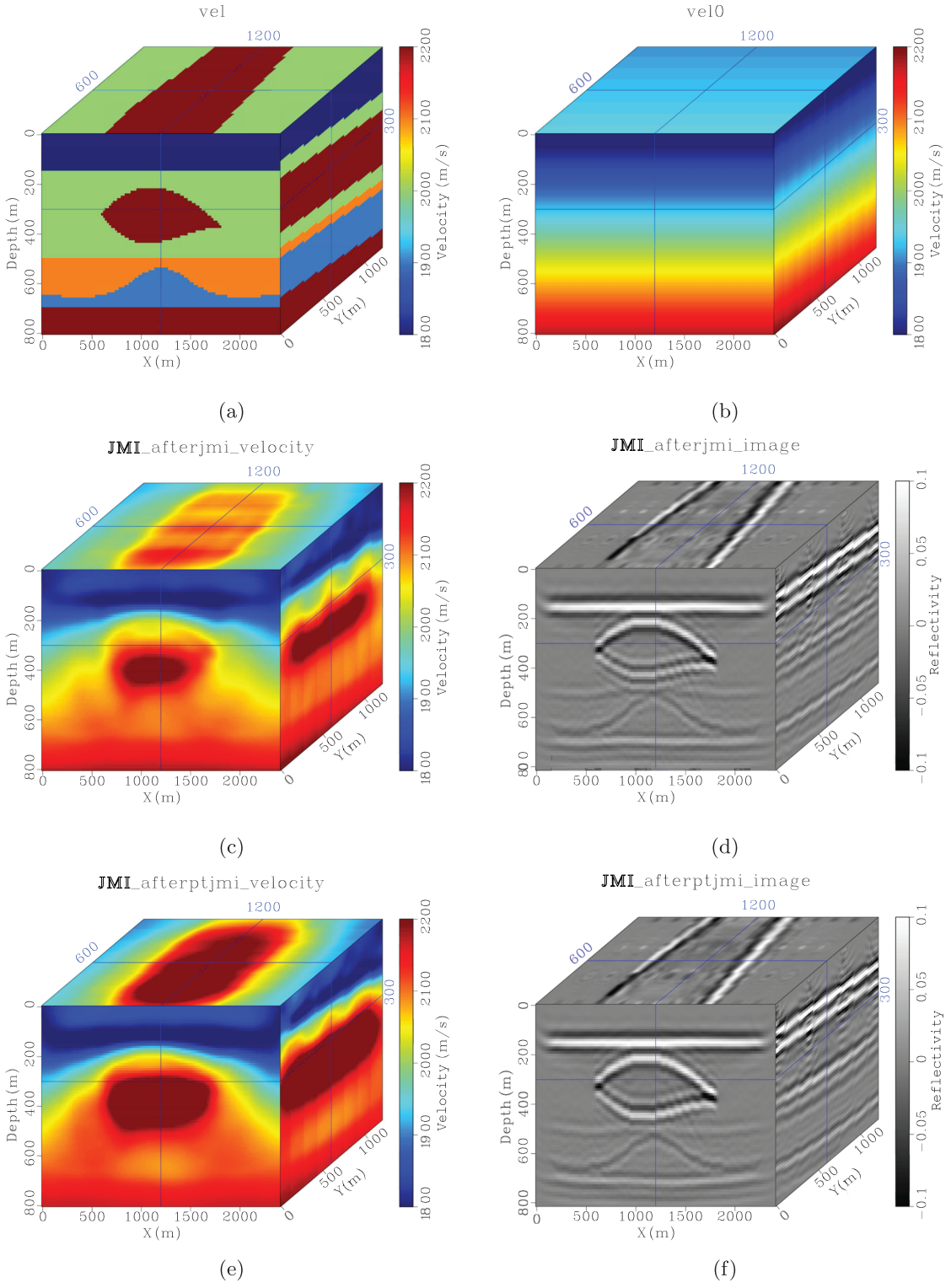

FIGURE 14 A 3D synthetic example: (a) and (b) the true and initial velocity; (c) and (d) the inverted velocity and reflectivities using depth JMI; (e) and (f) the inverted velocity and reflectivities using pseudo-time JMI. Note that one extra round of depth JMI is applied after pseudo time JMI.

200 and 20 m; the crossline source and receiver spacings are 400 and 20 m. We use a Ricker wavelet with a 20-Hz peak frequency, and the frequency bandwidth during JMI is 5–30 Hz. A gradient descent scheme with 45 iterations is applied in a multi-scale way for both depth and pseudo-time JMI. The initial velocity model is shown in Figure 14b, and the initial reflectivities are zero. The inverted models via 3D depth JMI and 3D pseudo-time JMI are shown in Figure 14c–f. We can observe that 3D pseudo-time JMI outperforms 3D depth JMI, especially in the overburden salt area. Note that, to further demonstrate the effectiveness of the pseudo-time JMI in 3D cases, more efforts should be made, for example, providing realistic and field 3D examples. However, it will be left for further research.

CONCLUSION

In the conventional depth joint migration inversion (JMI), when the velocity model is being updated, the reflectors in the estimated image are shifting accordingly. This might lead to non-robustness of the inversion. To avoid this issue, we propose a more robust JMI scheme, which parameterizes the models in vertical time, termed pseudo-time JMI. In this way, the updates of the velocity during inversion will not result in the associated location changes of reflectors. Instead, the focusing of the image improves gradually. The effectiveness of the proposed method has been demonstrated with two-dimensional (2D) and three-dimensional synthetic examples and a 2D marine field dataset from the Vøring basin in Norway. In all examples, the inverted models using pseudo-time JMI show clear improvements compared to depth JMI. One main limitation of the proposed pseudo-time JMI is the simple linear assumption in the depth-pseudo-time conversion process. This assumption might cause some artefacts in the converted models, especially in the presence of strong lateral velocity variations in the subsurface. To resolve this issue, one subsequent round of depth JMI is recommended in the case of strong lateral velocity variations.

ACKNOWLEDGEMENTS

The authors thank the sponsors of the Delphi consortium for their support, Aramco Overseas Company for providing the two-dimensional deep water model and Equinor for providing the field data from the Vøring basin.

DATA AVAILABILITY STATEMENTS

The data that support the findings of this study are available from Aramco Overseas Company or Equinor. Restrictions apply to the availability of these data, which were used under license for this study. Data are available from the authors with the permission of Aramco Overseas Company or Equinor.

ORCID

Shan Qu https://orcid.org/0000-0003-3951-9355

REFERENCES

Alasmri, H. & Verschuur, D.J. (2019) Towards Q-compensation in full wavefield migration and joint migration inversion. In: *81st EAGE annual conference & exhibition*, volume 2019. Houten, The Netherlands: European Association of Geoscientists & Engineers, pp. 1–5.

Alshuhail, A.A. & Verschuur, D.J. (2019) Robust estimation of vertical symmetry axis models via joint migration inversion: including multiples in anisotropic parameter estimation. *Geophysics*, 84(1), C57–C74.

Berkhout, A.J. (2014a) Review paper: An outlook on the future of seismic imaging, Part I: forward and reverse modelling. *Geophysical Prospecting*, 62(5), 911–930.

Berkhout, A.J. (2014b) Review paper: An outlook on the future of seismic imaging, Part II: Full-wavefield migration. *Geophysical Prospecting*, 62(5), 931–949.

Berkhout, A.J. (2014c) Review paper: An outlook on the future of seismic imaging, Part III: Joint migration inversion. *Geophysical Prospecting*, 62(5), 950–971.

Davydenko, M., Verschuur, D. & Berkhout, A. (2014) Omnidirectional extension of full wavefield migration. In: *76th EAGE annual conference & exhibition*, volume 2014. Houten, The Netherlands: European Association of Geoscientists & Engineers, pp. 1–5.

Davydenko, M. & Verschuur, D.J. (2017a) Full-wavefield estimation of angle-dependent reflectivity and migration velocity. In: *87th annual international meeting*. SEG Technical Program Extended Abstract 2017. Houston, TX: Society of Exploration Geophysicists, pp. 5631–5635.

Davydenko, M. & Verschuur, D.J. (2017b) Full-wavefield migration: using surface and internal multiples in imaging. *Geophysical Prospecting*, 65(1), 7–21.

Eisenberg, G., Schuenemann, E., Gierse, G., Verschuur, E. & Qu, S. (2019) Robust velocity estimation via joint migration inversion and full waveform inversion. In: *89th annual international meeting*. SEG Technical Program Extended Abstracts 2019. Houston, TX: Society of Exploration Geophysicists, pp. 1224–1228.

Gazdag, J. (1978) Wave equation migration with the phase-shift method. *Geophysics*, 43(7), 1342–1351.

Ma, X. & Alkhalifah, T. (2012) Wavefield extrapolation in pseudo-depth domain. In: *74th EAGE conference & exhibition incorporating EUROPEC 2012*, volume 2012. Houten, The Netherlands: European Association of Geoscientists & Engineers, pp. 1MA–Z51.

Ma, X. & Alkhalifah, T. (2013) Wavefield extrapolation in pseudodepth domain. *Geophysics*, 78(2), S81–S91.

Operto, S., Ravaut, C., Improta, L., Virieux, J., Herrero, A. & Dell'Aversana, P. (2004) Quantitative imaging of complex structures from dense wide-aperture seismic data by multiscale traveltime and waveform inversions: a case study. *Geophysical Prospecting*, 52(6), 625–651.

Plessix, R., Milcik, P., Corcoran, C., Kuehl, H. & Matson, K. (2012) Full waveform inversion with a pseudotime approach. In: *74th EAGE conference and exhibition incorporating EUROPEC 2012*, volume 2012. Houten, The Netherlands: European Association of Geoscientists & Engineers, pp. cp-293–00717.

Plessix, R.-É. (2013) A pseudo-time formulation for acoustic full waveform inversion. *Geophysical Journal International*, 192(2), 613–630.

Plessix, R.-E., Baeten, G., de Maag, J.W., Klaassen, M., Rujie, Z. & Zhifei, T. (2010) Application of acoustic full waveform inversion to a low-frequency large-offset land data set. In: *80th annual international meeting*. SEG Technical Program Extended Abstracts 2010. Houston, TX: Society of Exploration Geophysicists, pp. 930–934.

Qu, S. (2020) "Simultaneous joint migration inversion as a high-resolution time-lapse imaging method for reservoir monitoring". PhD thesis, Delft University of Technology.

Qu, S., Van den Brule, Y. & Verschuur, D. (2020) A stable scheme of joint migration inversion in the pseudo-time domain. In: *82nd EAGE annual conference & exhibition*, volume 2020. Houten, The Netherlands: European Association of Geoscientists & Engineers, pp. 1–5.

Qu, S. & Verschuur, D. (2021) An effective scheme of pseudo-time joint migration inversion with an AVO mitigating workflow. In: *83rd EAGE annual conference & exhibition*, volume 2021. Houten, The Netherlands: European Association of Geoscientists & Engineers, pp. 1–5.

Qu, S. & Verschuur, D.J. (2020) Simultaneous joint migration inversion for high-resolution imaging/inversion of time-lapse seismic datasets. *Geophysical Prospecting*, 68, 1167–1188.

Staal, X.R. (2015) "Combined imaging and velocity estimation by Joint Migration Inversion". PhD thesis, Delft University of Technology.

Staal, X.R. & Verschuur, D.J. (2013) Joint migration inversion, imaging including all multiples with automatic velocity update. In: *75th EAGE conference & exhibition incorporating SPE EUROPEC 2013*, volume 2013. European Association of Geoscientists & Engineers, pp. cp-348–00920.

Sun, Y., Kim, Y., Qu, S., Verschuur, D., Almomin, A. & van Borselen, R. (2018a) Joint migration inversion versus FWI-RTM – a comparison study on a 2D realistic deep water model. In: *80th conference and exhibition*. Houten, The Netherlands: European Association of Geoscientists & Engineers, pp. 1–5.

Sun, Y., Kim, Y., Qu, S. & Verschuur, E. (2019) Joint migration inversion versus FWI-RTM: A comprehensive comparison study based upon 2D realistic offshore models. In: *International petroleum technology conference*, Beijing, China, March 2019. Kuala Lumpur, Malaysia: International Petroleum Technology Conference.

Sun, Y., Kim, Y.S., Qu, S., Verschuur, E., Almomin, A. & van Borselen, R. (2018b) Angle-dependent full wavefield migration based upon full waveform inversion and joint migration inversion. In: *88th annual international meeting*. SEG Technical Program Extended Abstracts 2018. Houston, TX: Society of Exploration Geophysicists, pp. 4357–4361.

Sun, Y., Verschuur, E. & Qu, S. (2019) Research note: Derivations of gradients in angle-independent joint migration inversion. *Geophysical Prospecting*, 67(3), 572–579.

Symes, W.W. (2008) Migration velocity analysis and waveform inversion. *Geophysical Prospecting*, 56(6), 765–790.

Tarantola, A. (1984) Inversion of seismic reflection data in the acoustic approximation. *Geophysics*, 49(8), 1259–1266.

van Groenestijn, G.J.A. & Verschuur, D.J. (2009) Estimating primaries by sparse inversion and application to near-offset data reconstruction. *Geophysics*, 74, A23–A28.

Verschuur, D. & Staal, X. (2014) Using primaries and multiples in time-lapse imaging and velocity estimation. In: *SEG technical program expanded abstracts 2014*. Houston, TX: Society of Exploration Geophysicists, pp. 4955–4959.

Verschuur, D.J., Staal, X.R. & Berkhout, A.J. (2016) Joint migration inversion: Simultaneous determination of velocity fields and depth images using all orders of scattering. *The Leading Edge*, 35(12), 1037–1046.

Virieux, J. & Operto, S. (2009) An overview of full-waveform inversion in exploration geophysics. *Geophysics*, 74(6), WCC127–WCC152.

Xu, S., Wang, D., Chen, F., Zhang, Y. & Lambare, G. (2012) Full waveform inversion for reflected seismic data. In: *74th EAGE conference and exhibition incorporating EUROPEC 2012*, volume 2012. Houten, The Netherlands: European Association of Geoscientists & Engineers, pp. cp-293–00729.

How to cite this article: Qu, S. & Verschuur, D.J. (2022) An effective scheme of joint migration inversion in the pseudo-time domain. *Geophysical Prospecting*, 1–15. https://doi.org/10.1111/1365-2478.13296